

# We are IntechOpen, the world's leading publisher of Open Access books Built by scientists, for scientists

6,900

Open access books available

186,000

International authors and editors

200M

Downloads

Our authors are among the

154

Countries delivered to

TOP 1%

most cited scientists

12.2%

Contributors from top 500 universities



WEB OF SCIENCE™

Selection of our books indexed in the Book Citation Index  
in Web of Science™ Core Collection (BKCI)

Interested in publishing with us?  
Contact [book.department@intechopen.com](mailto:book.department@intechopen.com)

Numbers displayed above are based on latest data collected.  
For more information visit [www.intechopen.com](http://www.intechopen.com)



# Nanoparticles and Nanostructures Fabricated Using Femtosecond Laser Pulses

Chih Wei Luo

*Department of Electrophysics, National Chiaotung University, Taiwan  
Republic of China*

## 1. Introduction

Recently, the processing of materials by femtosecond (fs) laser pulses has attracted a great deal of attention, because fs pulse energy can be precisely and rapidly transferred to the materials without thermal effects (Stuart et al., 1995). In particular, periodic microstructures can be produced in almost any materials using fs pulses directly and without the need for masks or chemical photoresists to relieve the environmental concerns. For instance, nanoripples (Hsu et al., 2007; Luo et al., 2008; Sakabe et al., 2009; Jia et al., 2010; Yang et al., 2010; Bonse & Krüger, 2010; Okamoto et al., 2010; Huang et al., 2009), nanoparticles (Jia et al., 2006; Luo et al., 2008; Teng et al., 2010), nanocones (Nayak et al., 2008), and nanospikes (Zhao et al., 2007b) have been induced in various materials using single-beam fs laser pulses in air. In addition, fs laser ablation for metals and semiconductors in a vacuum environment (Amoruso et al., 2004; Liu et al., 2007a) and in liquid (Tsuji et al., 2003) have also been extensively investigated. These results are a strong indicator of the application potential of fs laser pulses in science and industry.

In this chapter, we demonstrate the generation of nanoparticles and nanostructures (including ripples and dots) using fs laser pulses. Initially, we selected the II-VI semiconductor ZnSe to demonstrate the fabrication of nanoparticles. Following the irradiation of fs laser pulses at a wavelength of 800 nm and pulse duration of 80 fs, many hexagonal-phase ZnSe nanoparticles formed on the surface of an undoped (100) cubic ZnSe single-crystal wafer. The interesting phase transition from the cubic structure of ZnSe single-crystal wafer to the hexagonal structure of ZnSe nanoparticles may have been caused by the ultra-high ablation pressure at the local area due to the sudden injection of high-energy leading to solid-solid transition. This chapter discusses the details of the mechanisms underlying this process.

In the second part of this chapter, we introduce controllable nanoripple and nanodot structures to high- $T_c$  superconducting  $\text{YBa}_2\text{Cu}_3\text{O}_7$  (YBCO) thin films. We also introduce the surface morphology of YBCO thin films under single-beam and dual-beam fs laser irradiation. The generation of periodic ripple and dot structures is determined by the application of laser fluence, the number of pulses, polarization and the incident angles of the laser beam. The period and orientation of ripples and even the size and density of dots can be controlled by these parameters.

## 2. Fabrication of hexagonal-phase ZnSe nanoparticles

Zinc selenide (ZnSe) has been studied extensively since the 1970s for implementation in II-VI semiconductors, due to its promising opto-electrical and electrical properties of direct wide band gap 2.7 eV at 300 K (Tawara et al., 1999; Dinger et al., 2000; Xiang et al., 2003). Over the last decade, the development of nanotechnologies has had a tremendous impact on industry and basic scientific research. The nanostructures of ZnSe, in particular, have attracted considerable attention recently (Tawara et al., 1999; Sarigiannis et al., 2002). Generally, crystalline ZnSe exhibits two structural phases, cubic and hexagonal. In ambient environments, the cubic phase is most often studied because the hexagonal structure is thermodynamically unstable (Sarigiannis et al., 2002; Che et al., 2004). In this section, we demonstrate the fabrication of hexagonal-phase ZnSe nanoparticles using femtosecond laser pulses and characterize their properties.

### 2.1 Experimental setup and procedure

In this study, the laser source plays an important role causing materials to undergo various changes. To reach the nonlinear region, a light source with high pulse energy is required. The seed pulses at 800 nm were produced using a mode-locked Ti:sapphire laser (Coherent-Micra10) pumped by a diode pump solid state laser (Coherent-Verdi). After being stretched to  $\sim 200$  ps, these pulses were synchronously injected into a Ti:sapphire regenerative amplifier (Coherent-Legend) pumped by a 5-kHz Nd:YLF laser and the amplified pulses (pulse energy  $\sim 0.4$  mJ) were recompressed to  $\tau_p \sim 80$  fs at sample surface.

Figure 1 shows the experimental setup used for the fabrication of ZnSe nanoparticles. A plano-convex fused silica cylindrical lens with the focal length of 100 mm was used to focus the femtosecond laser pulses into a line spot ( $2270 \mu\text{m} \times 54 \mu\text{m}$ ). The (100) cubic ZnSe single-crystal wafers were mounted on a motorized X-Y-Z translation stage in air and scanned using the focused laser spot at the scanning speed of  $100 \mu\text{m/s}$  as shown in Fig. 1. The pulse energy was varied using metallic neutral density filters with OD0.1-OD2 (Thorlabs ND series).

Following femtosecond laser irradiation, a white-yellow powder [as shown in the inset of Fig. 2(b)], i.e. ZnSe nanoparticles, was observed on the surface of a ZnSe single-crystal wafer. Depending on the experimental objectives, these ZnSe nanoparticles could be dissolved in ethanol with ultrasonic waves or picked up with Scotch tape. After removing

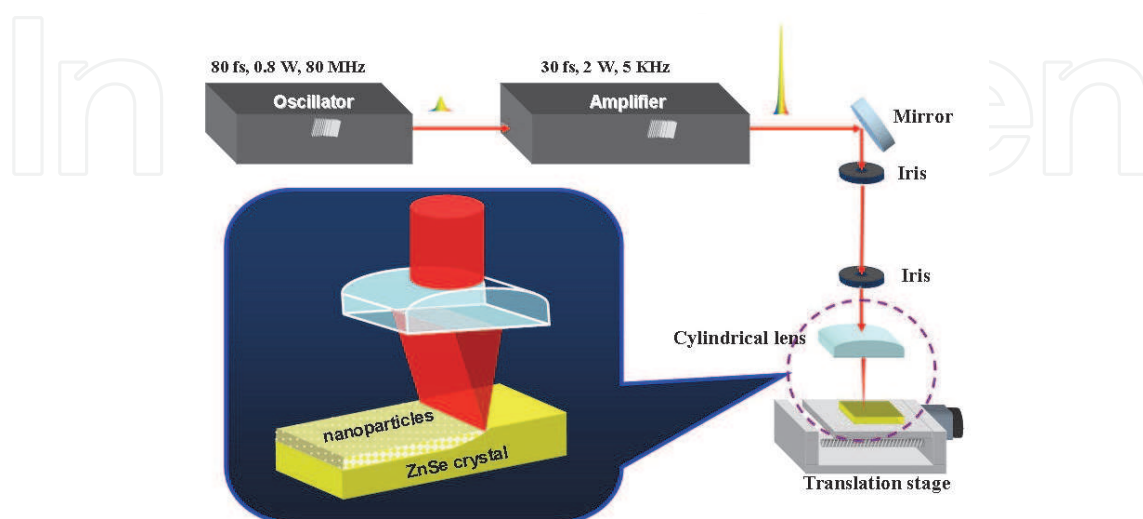


Fig. 1. Experimental setup for the fabrication of ZnSe nanoparticles.

the ZnSe nanoparticles from the surface of a ZnSe single-crystal wafer, many sub-wavelength ripples were observed on the surface, as shown in Fig. 2(b). These ripples appeared perpendicular to the scanning direction of the laser beam and the polarization of laser pulses, which are presented by the dashed and solid arrows, respectively, in Fig. 2(b).

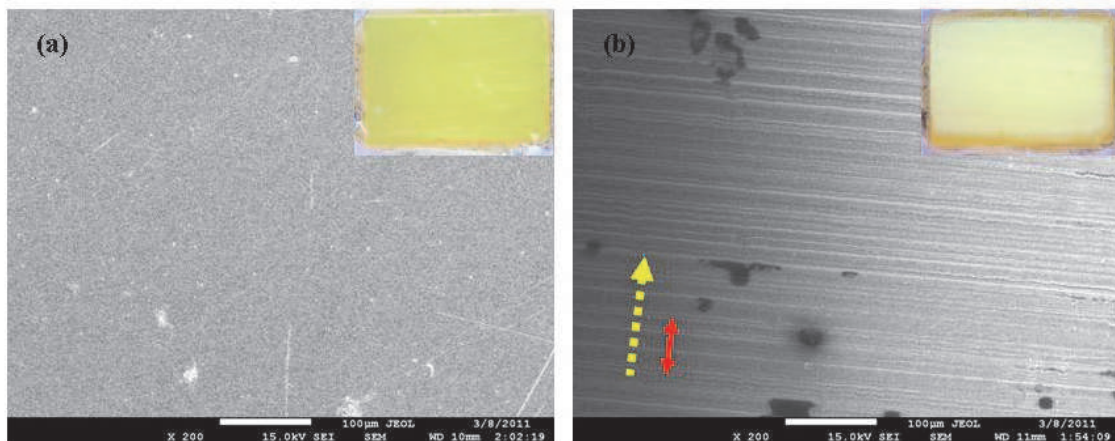


Fig. 2. SEM images of ZnSe single-crystal wafers; (a) before; and (b) after femtosecond laser pulse irradiations. Inset: OM images of ZnSe single-crystal wafer; (a) before; and (b) after femtosecond laser pulse irradiations. The dashed arrow indicates the scanning direction of a laser beam. The solid arrow indicates the polarization of laser pulses.

## 2.2 Characteristics of ZnSe nanoparticles

Figure 3(a) shows X-ray diffraction patterns of ZnSe nanoparticles fabricated at various fluences, which can be indexed by the hexagonal structure according to the JCPDS card no.80-0008 for ZnSe ( $a = b = 3.974 \text{ \AA}$ ,  $c = 6.506 \text{ \AA}$ ). It can be clearly seen that the cubic phase of the ZnSe single-crystal wafers has been transferred to the hexagonal phase in the ZnSe nanoparticles. Because hexagonal ZnSe is a metastable phase under ambient conditions, it can only be fabricated under the very strict growth conditions (Jiang et al., 2004; Liu et al., 2007b). However, hexagonal ZnSe nanoparticles can be easily and reliably achieved using femtosecond laser ablation as demonstrated in this study. Additionally, Figure 3(b) shows the room-temperature Raman scattering spectra of the ZnSe wafer, before and after the laser irradiation, and fabricated nanoparticles. The Raman peak at  $252 \text{ cm}^{-1}$  can be assigned to the longitudinal optical (LO) phonon mode of the cubic structure observed both in the ZnSe wafer before and after laser processing. For ZnSe nanoparticles, a strong peak appears at  $234 \text{ cm}^{-1}$  which is the so-called surface phonon mode (Shan et al., 2006). Typically, this surface phonon mode is a characteristic feature of nanostructures due to their large surface to volume ratio. Besides, no LO phonon mode of cubic structure is observed in ZnSe nanoparticles indicating that the crystal structure of ZnSe nanoparticles is pure hexagonal phase which is in accord with the X-ray diffraction patterns shown in Fig. 3(a).

Figure 4(a) shows a typical TEM image of ZnSe nanoparticles with the smooth spherical shape. A high-resolution TEM image at the atomic scale for one ZnSe nanoparticle is presented in the inset of Fig. 4(b). Furthermore, the six-fold electron diffraction pattern can be clearly observed in Fig. 4(b). Through the analysis of distance and angles between the nearest diffraction points and the center (biggest) point, the crystal structure of ZnSe nanoparticles was identified as a hexagonal and the orientation of each diffraction point is

marked in Fig. 4(b), which consists with the results of XRD in Fig. 3(a). The energy dispersive spectroscopy (EDS) spectrum in the inset of Fig. 4(a) illustrates the composition of these ZnSe nanoparticles, comprising only two elements of Zn and Se. This reveals that the high purity of hexagonal ZnSe nanoparticles can be reliably and simply fabricated using femtosecond laser pulses.

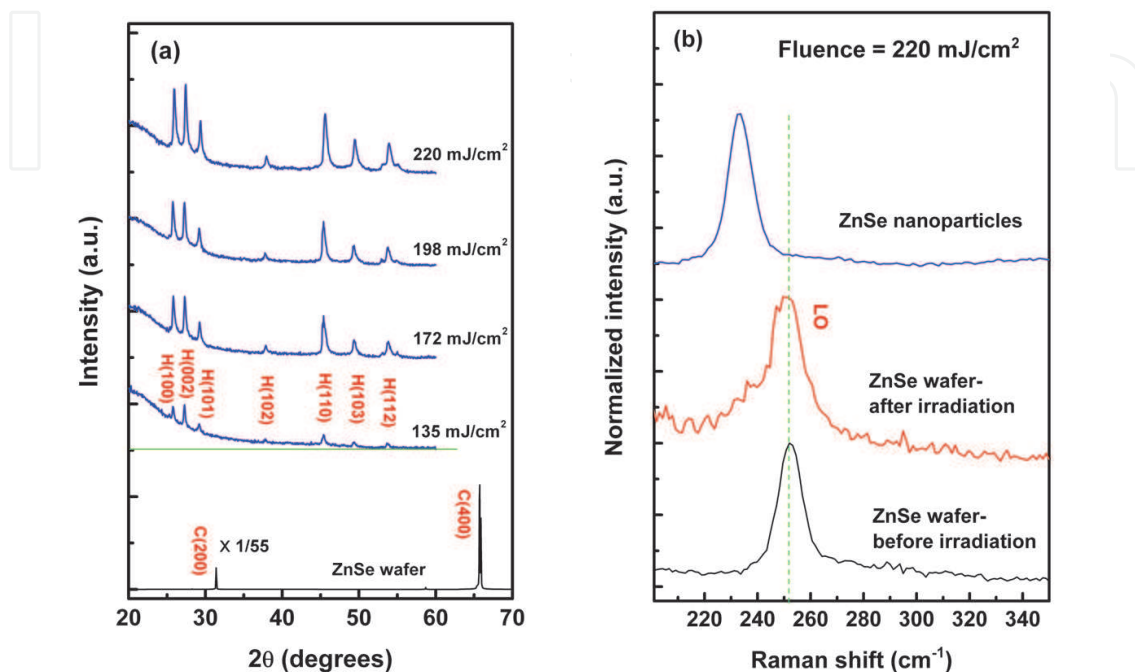


Fig. 3. (a) X-ray diffraction patterns of ZnSe wafer and ZnSe nanoparticles fabricated at various laser fluences. H: Hexagonal. C: Cubic. (b) Raman spectra of ZnSe wafer and ZnSe nanoparticles fabricated at the fluence of 220 mJ/cm². The 632.8 nm line of laser with 0.33 mW was used as the excitation light.

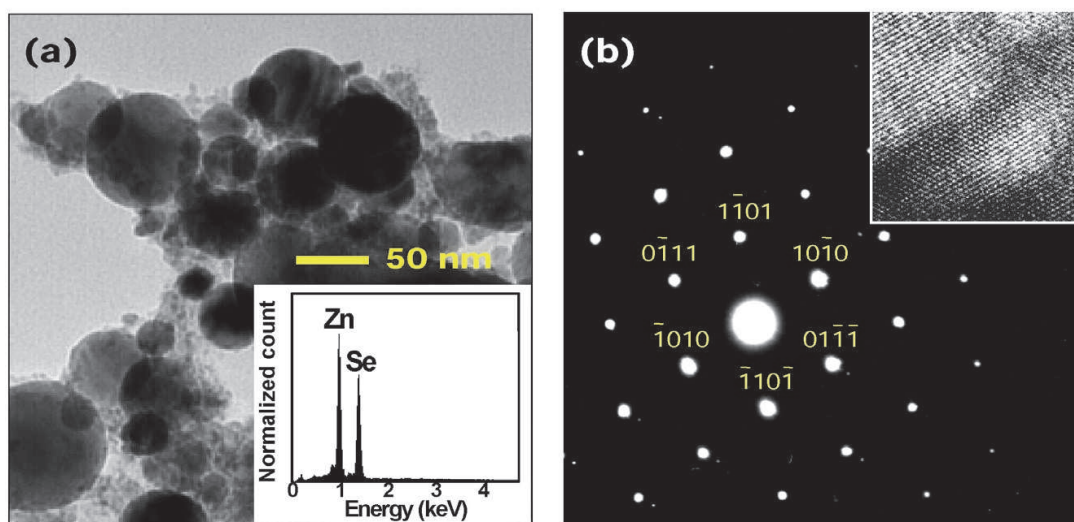


Fig. 4. (a) TEM images of ZnSe nanoparticles fabricated by the fluence of 220 mJ/cm². (b) TEM diffraction patterns of ZnSe nanoparticles in (a). Insets: (a) The EDS spectrum shows the composition of ZnSe nanoparticles; (b) High-resolution TEM image at the atomic scale.

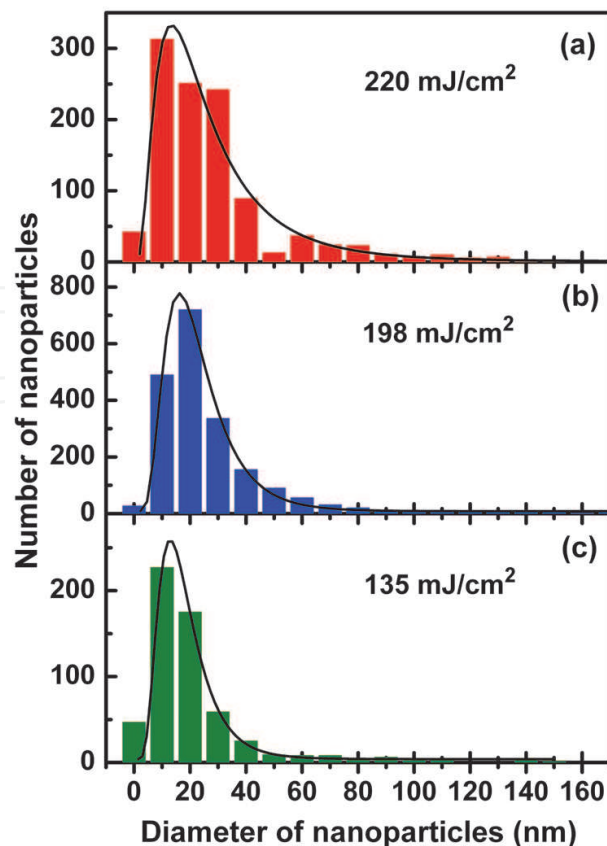


Fig. 5. Size distribution of ZnSe nanoparticles at various laser fluences corresponding to the TEM images in Fig. 4(a) with an area of  $3.2 \mu\text{m} \times 2.6 \mu\text{m}$ . The solid lines are the log-normal fitting.

The size distribution of ZnSe nanoparticles fabricated at various fluences was analyzed in Fig. 5. By the fitting of the log-normal function, we determined that the average diameter of ZnSe nanoparticles was approximately 16 nm in the case of  $135 \text{ mJ}/\text{cm}^2$ . With an increase in the laser fluence to  $198 \text{ mJ}/\text{cm}^2$  and  $220 \text{ mJ}/\text{cm}^2$ , the average size of the ZnSe nanoparticles increased to 20 nm and 22 nm, respectively. This indicates that the size of ZnSe nanoparticles can be controlled by laser fluence. Furthermore, the generation rate of ZnSe nanoparticles using fs laser pulses is approximately  $3.63 \times 10^{10} \text{ s}^{-1}$  (or  $7.26 \times 10^6$  per pulse) with a fluence of  $135 \text{ mJ}/\text{cm}^2$ . For the higher fluence of  $220 \text{ mJ}/\text{cm}^2$ , the generation rate of ZnSe nanoparticles increased by one order of magnitude to  $3.63 \times 10^{11} \text{ s}^{-1}$  (or  $7.26 \times 10^7$  per pulse).

### 2.3 Mechanism underlying the formation of hexagonal ZnSe nanoparticles

During femtosecond laser irradiation, a large amount of energy is transferred to the specimens thereby inducing dense plasma on the surface of the sample. However, the duration of energy transfer ( $\sim 80 \text{ fs}$ ) is too short for the lattice and the energy is only absorbed by the electrons within the extremely short interaction time. The ablated plume is confined within the laser focused position of the laser by the surrounding air. Thus, the rapidly cooling leads to the formation of nanoparticles on the surface of samples within the ablated plume to avoid a reaction with the air. That is the reason for the lack of impurities in the ZnSe nanoparticles fabricated by fs laser pulses in a study.

According to the early research, ZnSe transforms from a cubic structure to the hexagonal structure when the temperature is above the transition temperature ( $T_{tr}$ ) of 1698 K (Rudolph et al., 1995). When ZnSe crystals are irradiated by the femtosecond laser pulses, the

temperature of the ZnSe crystals increases. In the case of pulse lasers, an increase in the transient temperature  $\Delta T$  in materials can be estimated according to the relationship of  $\Delta T = W/(C \times V)$ , where  $W$  is the pulse energy,  $C$  is the heat capacity, and  $V$  is the illuminated volume. For ZnSe at 300 K,  $C$  is  $1.89 \times 10^6$  J/m<sup>3</sup>K (Martienssen & Warlimont, 2005),  $V$  is  $2.29 \times 10^{-13}$  m<sup>3</sup> [absorption depth  $\sim 1.87$   $\mu\text{m}$  estimated from the nonlinear absorption coefficient  $\beta$  (Tseng et al., 1996)], and  $W$  is on the order of 0.243 mJ (which is assumed to be totally absorbed by ZnSe). Thus, the  $\Delta T$  is approximately 560 K, which is far below the structural transition temperature of 1698 K. Therefore, a structural transition could not be induced by the increase in temperature. To identify the mechanism underlying the phase transition of ZnSe from cubic to hexagonal, we further analyzed the influence of “ablation pressure” (Batani et al., 2003), which has been studied from various perspectives over the past few decades (Key et al., 1980; Groot et al., 1992). When solids are irradiated by laser pulses, high-density plasma is formed on the surface of the samples. The compressed plasma in laser driven implosions has been characterized as the ablating or exploding pusher according to the surface ablation pressure and bulk pressure due to the preheating through electrons.

In 2003, Batani et al. (Batani et al., 2003) derived the shock pressure with the laser and target parameters expressed as

$$P(\text{Mbar}) = 11.6 \left( \frac{I}{10^{14}} \right)^{\frac{3}{4}} \lambda^{-\frac{1}{4}} \left( \frac{A}{2Z} \right)^{\frac{7}{16}} \left( \frac{Z \times t}{3.5} \right)^{-\frac{1}{8}} \quad (1)$$

where  $I$  is the laser intensity on target with the unit of W/cm<sup>2</sup>,  $\lambda$  is the laser wavelength in  $\mu\text{m}$ ,  $A$  and  $Z$  are, respectively, the mass number and the atomic number of the target, and  $t$  is the time in ns. Figure 6 shows the effective pressure in the irradiated region with the laser

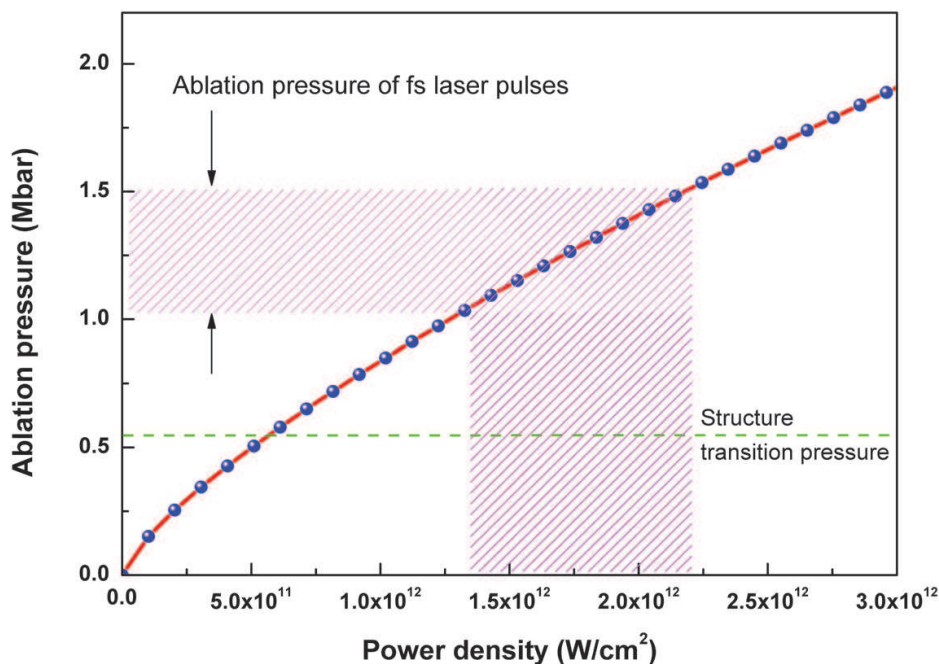


Fig. 6. Simulated ablation pressure as a function of the laser peak power density according to the Eq. (1). The shadow area indicates the range of laser peak power density in this study and corresponding ablation pressure. The dashed line represents the pressure of cubic-hexagonal phase transition, was obtained from ref. (Greene et al., 1995).

peak power density of the laser of  $0 \sim 3.0 \times 10^{12}$  W/cm<sup>2</sup>. In this study, the maximum pressure induced by the laser reached approximately 1.5 Mbar. According to the studies of Greene et al. in II-VI compounds (Greene et al., 1995), the solid-solid transition point, i.e. the cubic-hexagonal phase transition, of ZnSe is approximately 0.55 Mbar. In our experiments, the ablation pressure induced by the femtosecond laser pulses on the ZnSe single crystals was in the range of 1.0 Mbar to 1.5 Mbar as shown in the shadow area of Fig. 6. This exceeds the solid-solid transition pressure 0.55 Mbar (the dashed line in Fig. 6). Therefore, the hexagonal-phase ZnSe nanoparticles transferred from the cubic phase may be caused by high ablation pressure resulting from the femtosecond laser pulses, and the accompanied increase in surface to volume ratio in the nanoparticles.

### 3. Generation of nanoripples and nanodots on YBCO

Issues related to energy have gradually gained in value and attracted attention around world and, the high- $T_c$  superconducting YBa<sub>2</sub>Cu<sub>3</sub>O<sub>7</sub> (YBCO) has potential as an alternative material for green energy applications, e.g. electric power cables, transformers, motors, electric power generators, magnetic levitation systems, due to its high critical current of 77 K. For commercialization, critical current is the key parameter, and fs laser pulses may provide a new avenue to enhance the critical current of YBCO thin films. In this section, we demonstrate the formation of laser-induced subwavelength periodic surface structures (LIPSS), such as ripples and dots, on YBCO thin films using femtosecond laser and characterize their properties.

#### 3.1 Preparation of YBCO thin films

The YBCO thin films used in this study were prepared by pulse laser deposition (PLD) with a KrF excimer laser operating at a repetition rate of 3-8 Hz with an energy density of 2-4 J/cm<sup>2</sup> as shown in the inset of Fig. 7(a). The oxygen partial pressure during deposition was maintained at 0.25 Torr, and the substrate temperature was maintained at 780-790 °C. After completion of the deposition process, the film was cooled to room temperature under 600 Torr of oxygen with the heater off. The thickness of the film was approximately 200 nm. As shown in the X-ray diffraction (XRD) pattern in Fig. 7(b), the YBCO films were (001)-oriented normal

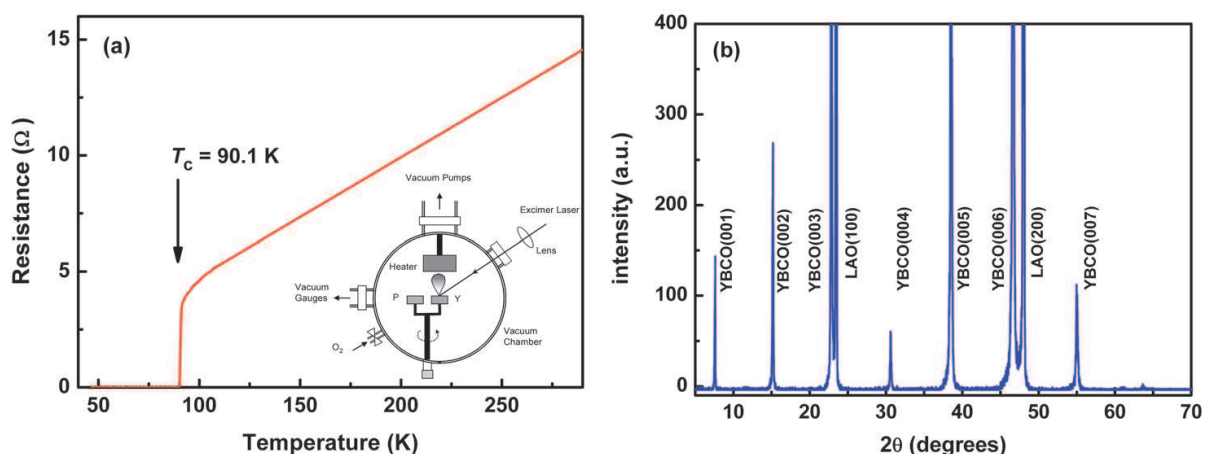


Fig. 7. (a) Resistance versus temperature curve measured on an as-deposited YBCO thin film. Inset: schematic illustration of the pulse laser deposition (PLD) system; (b) X-ray diffraction pattern of an as-deposited YBCO thin film.

to the (100)  $\text{LaAlO}_3$  (LAO) substrate. The temperature-dependent resistance of an (001)-oriented YBCO thin film was measured using the standard four-probe configuration as shown in Fig. 7(a). The resistance decreased linearly with temperature in the normal state and then dropped sharply to a zero-resistance superconducting state at 90.1 K. Both features are consistent with the XRD results, indicating the high quality of the YBCO films.

### 3.2 Generation of YBCO ripple structures

Figure 8 shows the optical system for generating ripple structures on the YBCO thin films. A commercial regenerative amplified Ti:sapphire laser (Legend USP, Coherent) with an 800-nm wavelength, 30-fs pulse duration,  $\sim 0.5$ -mJ pulse energy, and 5-kHz repetition rate was used as the irradiation source. After passing through a variable neutral density (ND) filter, the normal incident laser beam was focused on the surface of the sample forming a spot of  $\sim 200$   $\mu\text{m}$  by means of a convex lens with a focal length of 50-mm. The number of pulses or irradiation time was precisely controlled by the electric shutter.

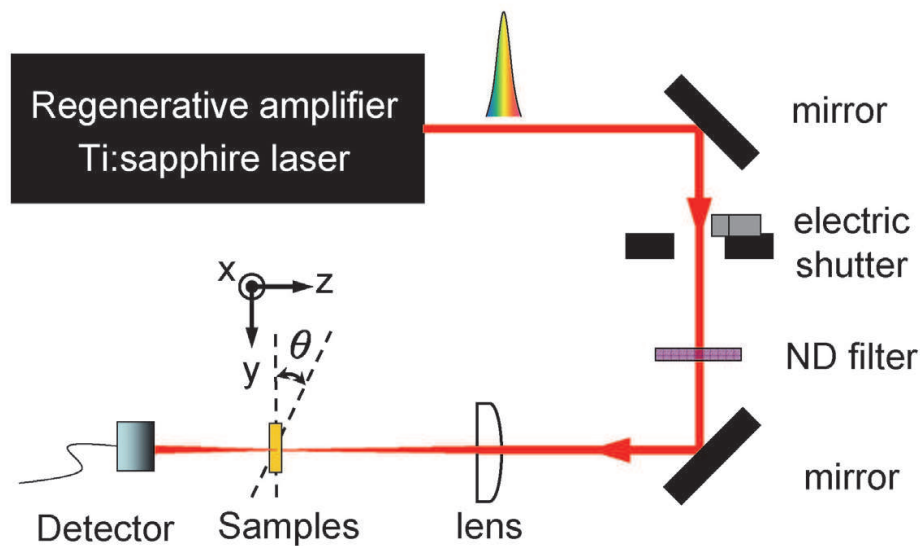


Fig. 8. Experimental setup for the generation of ripple structures on YBCO thin films.

SEM analysis (Fig. 9) indicates that the morphology of fs laser-induced surface structures depend strongly on the laser fluence. Figures 9(a)-9(f) show the evolution of the ripple structure on YBCO thin films irradiated by a single-beam fs laser with various laser fluences ( $F$ ) and a fixed number of pulses ( $N=600,000$ ). With an increase in laser fluence, the ripple structure becomes clear in SEM images, as evidenced by the appearance of satellite peaks in the 2D Fourier spectra in the insets of Figs. 9(c)-9(f) [there are no satellite peaks in the inset of Fig. 9(b) for the case of low laser fluence]. The spatial period  $\Lambda$  of ripples, estimated from the position of a satellite peak in the 2D Fourier spectra, was dependent on the laser fluence, as shown in Fig. 11(a). Once the laser fluences  $\geq 154$   $\text{mJ}/\text{cm}^2$ , the ripple period remained at approximately 517 nm. Furthermore, the “periodicity” of the ripple-like structures was approximately 500 nm, which is much smaller than either the spot size or the wavelength of the femtosecond laser, indicating that the pattern was not formed by simple plow-and-deposit processes.

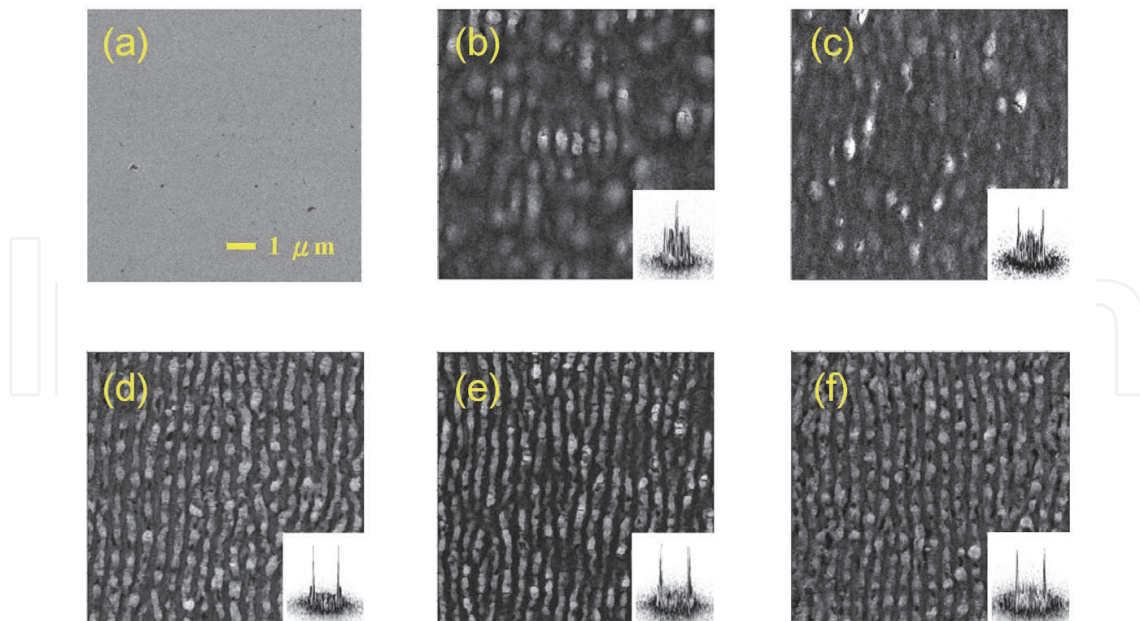


Fig. 9. Morphological evolution of structures on YBCO thin films induced by linear polarized fs laser with fixed number of pulses  $N=600,000$  and various fluences (a)  $F = 0$   $\text{mJ}/\text{cm}^2$ , (b)  $F = 43$   $\text{mJ}/\text{cm}^2$ , (c)  $F = 59$   $\text{mJ}/\text{cm}^2$ , (d)  $F = 79$   $\text{mJ}/\text{cm}^2$ , (e)  $F = 154$   $\text{mJ}/\text{cm}^2$ , (f)  $F = 319$   $\text{mJ}/\text{cm}^2$ . Inset: 2D Fourier spectra transferred from their corresponding SEM images ( $10\ \mu\text{m} \times 10\ \mu\text{m}$  with pixel resolution of  $\sim 0.04$  nm). The scale bar is applied to all pictures.

Figures 10(a)-10(c) show the evolution of the ripple structure on YBCO thin films irradiated by a single-beam fs laser with various numbers of pulses ( $N$ ) and the fixed laser fluence  $F = 79$   $\text{mJ}/\text{cm}^2$ . With an increase in the number of pulses, the ripple structure became increasingly clear in SEM images, as evidenced by the appearance of satellite peaks in the 2D Fourier spectra in the insets of Figs. 10(b) and 10(c) [there are no satellite peaks in the inset of Fig. 10(a) for an as-deposited YBCO thin film]. The spatial period of ripples, estimated from the position of satellite peaks in the 2D Fourier spectra, is independent of the number of pulses or irradiation time, as shown in Fig. 11(b). Once the number of pulses  $\geq 50,000$ , i.e. the sample surface was irradiated by the  $75$   $\text{mJ}/\text{cm}^2$  laser pulses for  $\geq 10$  s, ripples can be clearly observed on the surface of the sample. In addition, the real-time evolution of the ripple structure appears in the transmission measurements in Fig. 10(d). In the case of  $F = 154$   $\text{mJ}/\text{cm}^2$ , the transmission power of the laser beam dramatically increased to within 2 s and then saturated after  $\sim 10$  s. Some specific points were marked at  $79$   $\text{mJ}/\text{cm}^2$  of Fig. 10(d), and corresponding SEM images are shown in Figs. 10(a), 10(b), and 10(c), respectively. At 0.1 s [i.e.  $N=500$  in Fig. 10(a)], there are almost no structures on the surface of YBCO thin films. However, the rippled structure can be observed at 10 s [i.e.  $N=50,000$  in Fig. 10(b)]; meanwhile, the transmission power dramatically increased due to the thinning of YBCO films inside the grooves. For an extended irradiation time of 30 s [i.e.  $N=150,000$  in Fig. 10(c)], the ripple structure does not change from that of Fig. 10(b), e.g. the spatial period of ripple as shown in Fig. 11(b), except for the contrast of grooves causing slight rise in transmission power in Fig. 10(d). Furthermore, the characteristics of changes in transmission power in Fig. 10(d) are independent of laser fluence. This indicates that the formation of ripple structures is very rapid, with only  $\sim 2$  s needed, and the formation processes is independent of laser fluence. Laser fluence only affects the spatial period of ripple structures, as shown in Fig. 11(a).

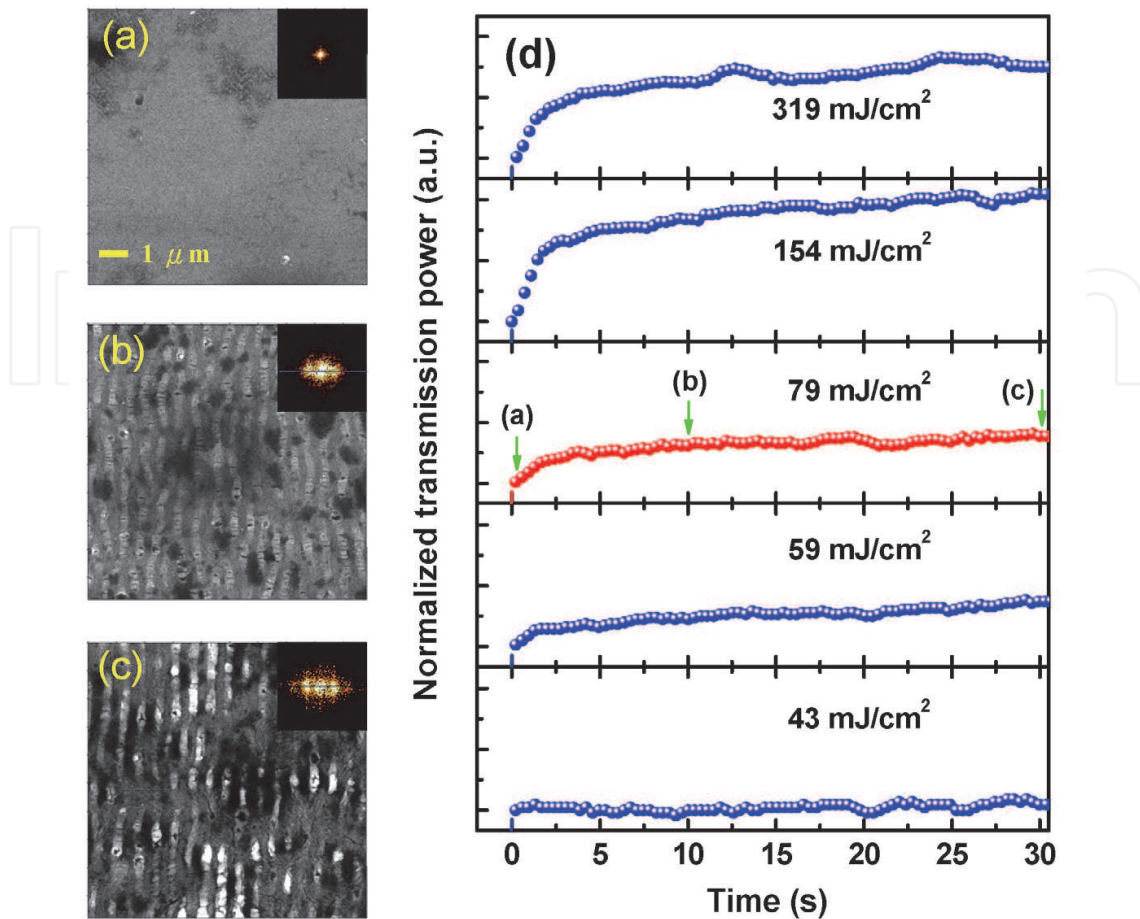


Fig. 10. Morphological evolution of structures on YBCO thin films induced by linear polarized fs laser with fixed laser fluence  $F = 79 \text{ mJ/cm}^2$  and various numbers of pulses (a)  $N = 500$ , (b)  $N = 50,000$ , (c)  $N = 150,000$ . (d) The transmission power of laser pulses as a function of irradiating time, *i.e.* pulse number  $N$ . Inset: 2D Fourier spectra which were transferred from their corresponding SEM images ( $10 \mu\text{m} \times 10 \mu\text{m}$  with pixel resolution of  $\sim 0.04 \text{ nm}$ ). The scale bar is applied to all pictures.

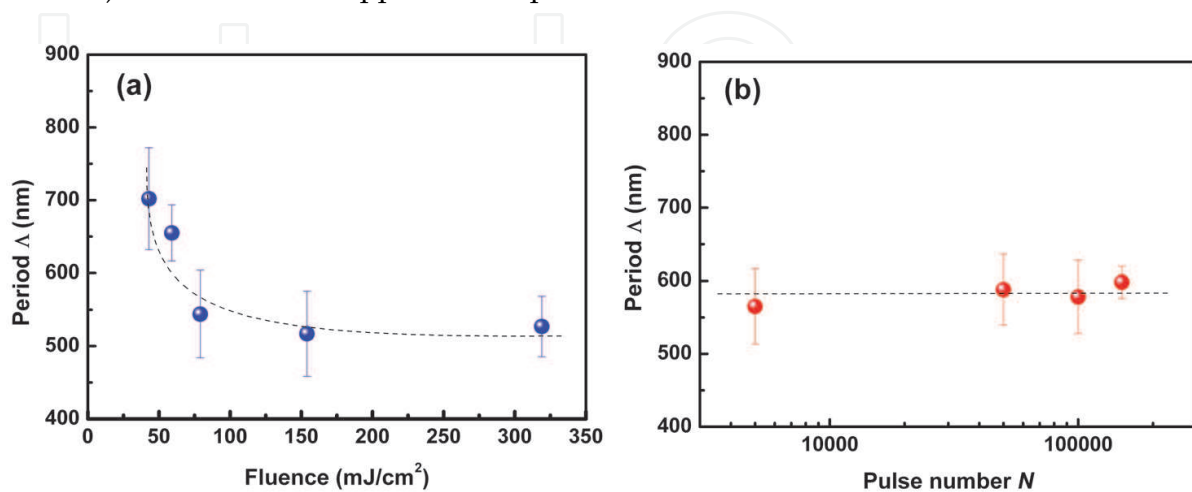


Fig. 11. (a) Dependence of the ripple period on the fluence. (b) Dependence of the ripple period on the number of pulses. The dashed lines are a guide to the eyes.

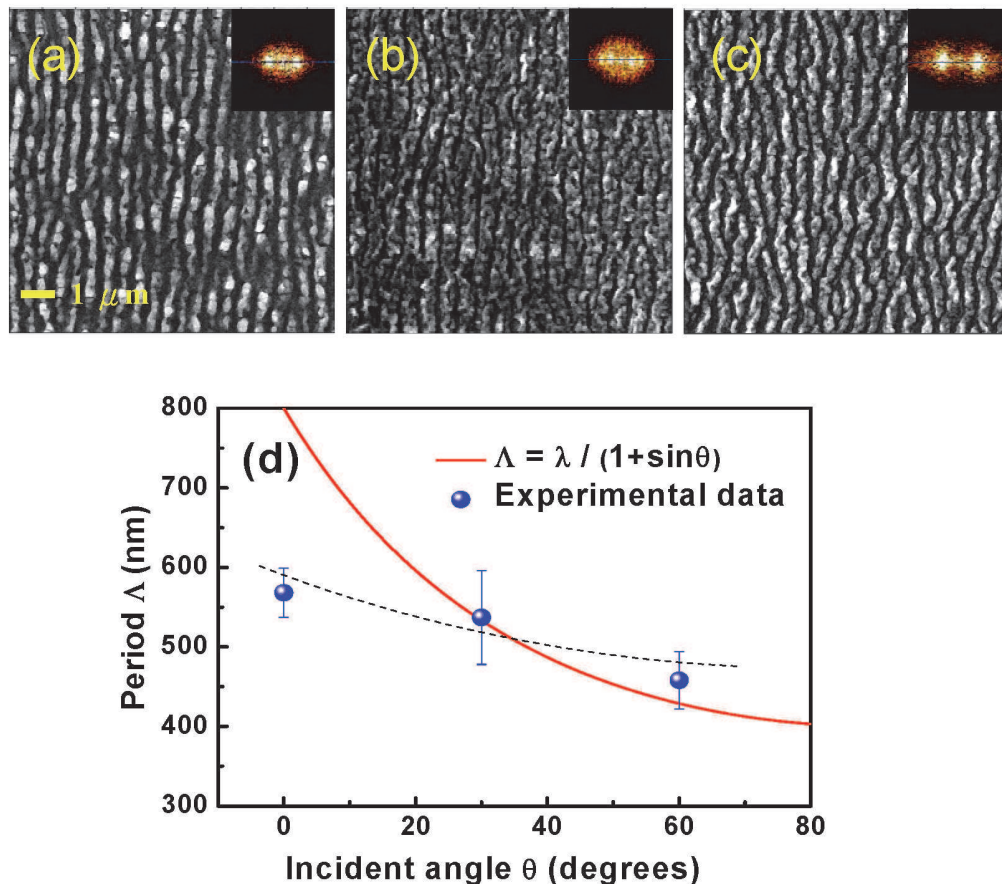


Fig. 12. Morphological evolution of ripple structures on YBCO thin films induced by linear polarized fs laser with  $F = 300 \text{ mJ/cm}^2$ ,  $N=150,000$ , and various incident angles (a)  $\theta = 0^\circ$ , (b)  $\theta = 30^\circ$ , (c)  $\theta = 60^\circ$ . (d) Dependence of the ripple period on the incident angle of laser pulses. The dashed lines are a guide to the eyes. All SEM images are  $10 \mu\text{m} \times 10 \mu\text{m}$  with pixel resolution of  $\sim 0.04 \text{ nm}$ .

On the other hand, with the fluence and pulse number fixed at  $\sim 300 \text{ mJ/cm}^2$  and 150,000, respectively, we found that the spatial period decreased with an increase in the incident angle ( $\theta$ ) [see Fig. 12(d)]. However, the observed period of ripple at  $\theta = 0^\circ$  was significantly smaller than the prediction of  $\Lambda = \lambda / (1 + \sin\theta)$  (Zhou et al., 1982). In addition, the incident angle-dependent period of ripples on YBCO thin films cannot be described using this simplified scattering model [the solid line in Fig. 12(d)]. Therefore, the influence of surface electromagnetic waves, i.e. surface plasmons (SPs) should be taken into account in the formation of subwavelength ripples (Sakabe et al., 2009; Huang et al., 2009). According to Shimotsuma's et al. results (Shimotsuma et al.; 2003), femtosecond incident light easily excites plasmons on the surface of various materials. As shown in Fig. 13(c), once the momentum conservation condition for the wave vectors of the linear polarized laser light ( $\mathbf{K}_i$ ), the plasma wave ( $\mathbf{K}_p$ ), and the laser-induced subwavelength periodic surface structures (LIPSS,  $\mathbf{K}_L$ ) is satisfied, such plasmons could couple with the incident light. The interference between the plasmons and the incident light would generate a periodically modulated electron density causing nonuniform melting. After irradiation with a femtosecond laser, the interference ripple was inscribed on the surface of the YBCO thin film.

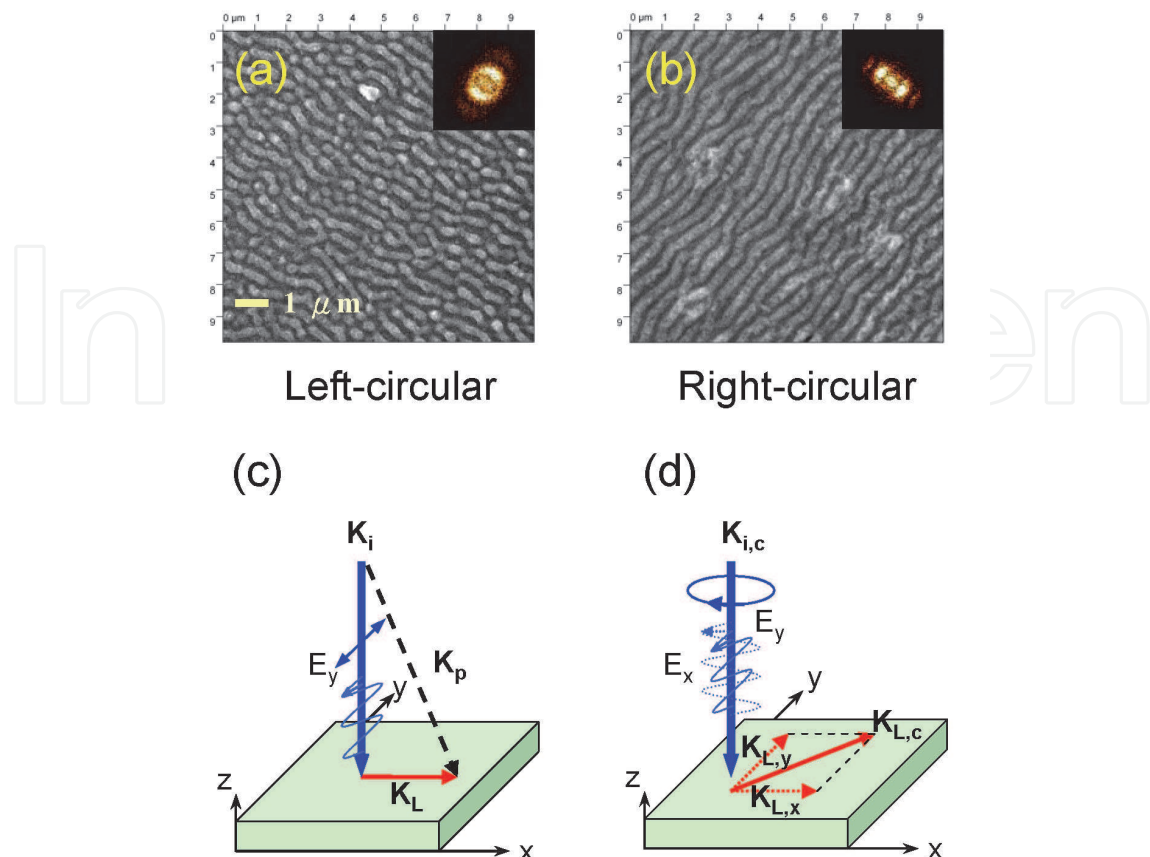


Fig. 13. SEM images ( $10\ \mu\text{m}\times 10\ \mu\text{m}$  with pixel resolution of  $\sim 0.04\ \text{nm}$ ) of fs LIPSS induced by (a) the left- and (b) right-circularly polarized beams; (c) Schematic of the momentum conservation condition of wave vectors of linear polarized laser light ( $\mathbf{K}_i$ ), plasma wave ( $\mathbf{K}_p$ ), and LIPSS ( $\mathbf{K}_L$ ); (d) Schematic processes of the LIPSS by circularly polarized laser light ( $\mathbf{K}_{i,c}$ ). The scale bar is applied to all pictures.

Interestingly, when we used a circularly polarized beam, the rippled structures were still produced, as shown in Figs. 13(a) and 13(b). The orientation of the ripples was set at  $-45^\circ$  and  $+45^\circ$  for left and right circularly polarized beams, respectively, with respect to the incident plane of the beam. In both cases, the spatial period was  $491\ \text{nm}$ , as produced by fs laser pulses with a fluence of  $185\ \text{mJ}/\text{cm}^2$  and number of pulses set to 150,000. These results show the orientation of rippled structures strongly depend on the polarization-state of incident fs pulses. These results are consistent with the results of Zhao et al. on tungsten (Zhao et al., 2007a, 2007b). In principle, circularly polarized light ( $\mathbf{K}_{i,c}$ ) can be decomposed to two perpendicular linear-polarization lights ( $E_x$  and  $E_y$ ) through retardation of  $\lambda/4$  in phase, as shown in Fig. 13(d). Linearly polarized light  $E_x$  and  $E_y$  can induce the LIPSS  $\mathbf{K}_{L,x}$  and  $\mathbf{K}_{L,y}$ , respectively, as long as the momentum conservation condition in Fig. 13(c) is satisfied. Thus, both  $\mathbf{K}_{L,x}$  and  $\mathbf{K}_{L,y}$  with phase coherent further cause the  $\mathbf{K}_{L,c}$  according to the momentum conservation condition of  $\mathbf{K}_{L,c} = \mathbf{K}_{L,x} + \mathbf{K}_{L,y}$ . The  $45^\circ$  wave vector of LIPSS,  $\mathbf{K}_{L,c}$  is completely consistent with the direction of the satellite peaks in the 2D Fourier spectra [the inset of Fig. 13(a)]. Namely, the orientation of ripples is  $-45^\circ$  for left-circularly polarized beams with respect to the incident plane of the beam. Similarly, right-circularly polarized beams induce a  $+45^\circ$  orientation of LIPSS,  $\mathbf{K}_{L,c}$ , according to the momentum conservation condition of  $\mathbf{K}_{L,c} = -\mathbf{K}_{L,x} + \mathbf{K}_{L,y}$  consistent with the results in Fig. 13(b).

### 3.3 Generation of YBCO dot structures

To produce dot structures on YBCO thin films, we adopted a dual-beam scheme using the modified Michelson interferometer shown in Fig. 14. The polarization of both beams was individually controlled by two quarter-wave plates before the reflection mirrors in both arms of the dual-beam setup. After the beam splitter in the dual-beam setup, both beams were collinearly and simultaneously focused on the surface of the sample using a convex lens with a focal length of 50-mm. Before generating the YBCO dot structures, we measured the interference patterns between two beams to check the temporal overlap of the two pulses. In the inset of Fig. 14, the interference pattern between the two pulses with parallel polarization can be clearly observed after adjusting the delay in one of the two pulses. The polarization of two pulses was set perpendicularly to each other to eliminate interference patterns and generate the YBCO dot structures. All experiments were performed in air under atmospheric pressure.

As shown in Figs. 15(a1)-15(d1), it is surprising that many dots rather than regular ripples appeared on the surface of YBCO thin films using a dual-beam setup with perpendicularly linear polarization. In the case of the dual-beam setup, the  $\mathbf{K}_{L,x}$  and  $\mathbf{K}_{L,y}$  without coherence in phase induced by random phase and perpendicularly linear-polarization beams ( $E_x$  and  $E_y$ ), respectively, would not satisfy the conservation of momentum of  $\mathbf{K}_{L,c} = \pm\mathbf{K}_{L,x} + \mathbf{K}_{L,y}$  and be unable to create  $\pm 45^\circ$  wave vector of LIPSS,  $\mathbf{K}_{L,c}$  as shown in Fig. 13(d). Therefore, the  $\mathbf{K}_{L,x}$  and  $\mathbf{K}_{L,y}$  which are perpendicular to each other would lead 2D nonuniform melting and further aggregation to form randomly distributed dots [see the 2D Fourier spectra in the inset of Figs. 15(a2)-15(d2)] due to surface tension. In the case of  $N = 25,000$ , the average diameter of dots was approximately 632 nm estimated by the log-normal fitting presented in Fig. 15(a2). An increase in the number of pulses resulted in a marked broadening in the size distribution, although the average size only slightly increased from 632 nm to 844 nm [see Figs. 15(a2)-15(d2)]. For  $N = 300,000$ , the size of a part of dots was on the order of micrometers. However, larger dots influence the dot density on the surface of YBCO thin films. For instance, the density of dots increases with the number of pulses  $\leq 150,000$ . Once the dots grow too large to merge with the nearest neighbors, or even next nearest neighbors, the density of the dots significantly shrank, as shown in Fig. 15(c1). In this manner, the size and density of YBCO dots can be controlled by the numbers of pulses from the fs laser.

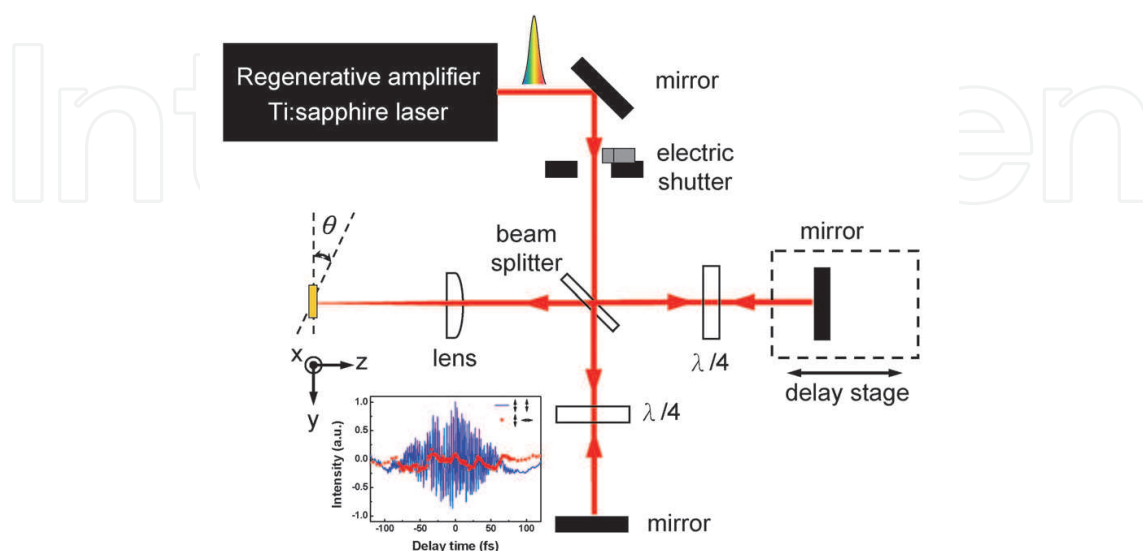


Fig. 14. Experimental setup for the generation of nanodots on YBCO thin films.

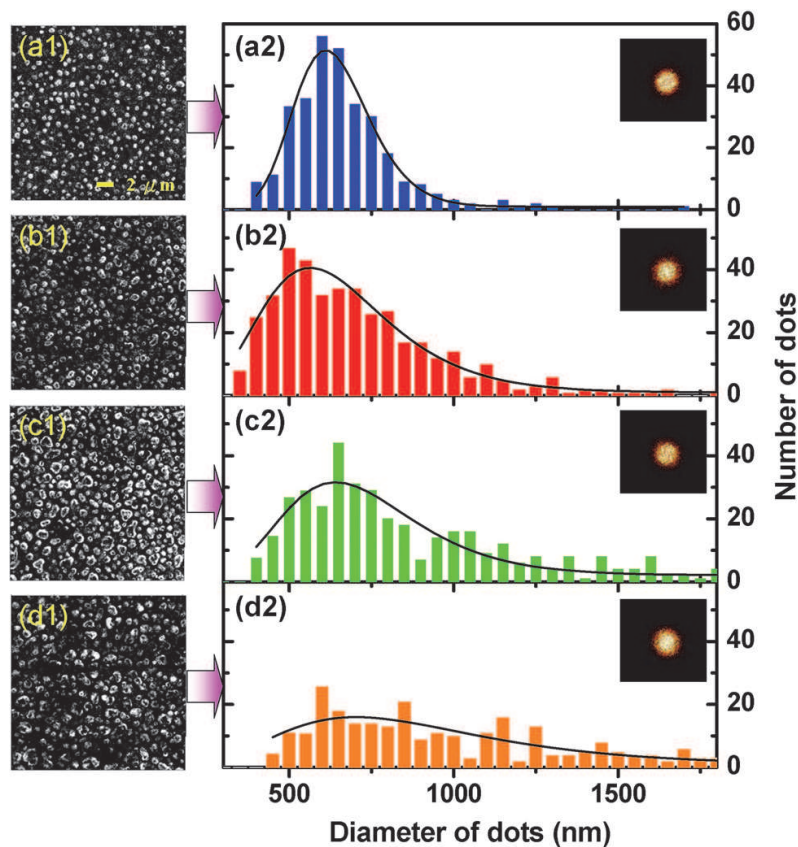


Fig. 15. Dot structures on YBCO thin films induced by a dual-beam setup with fluence = 87 mJ/cm<sup>2</sup> and various numbers of pulses (a1)  $N = 25,000$ , (b1)  $N = 50,000$ , (c1)  $N = 150,000$ , (d1)  $N = 300,000$ . (a2)-(d2) The size distribution corresponds to the SEM images (10  $\mu\text{m} \times 10 \mu\text{m}$  with pixel resolution of  $\sim 0.04 \text{ nm}$ ) (a1)-(d1), respectively. Solid lines are the log-normal fitting. Inset: 2D Fourier spectra which were transferred from their corresponding SEM images (a1)-(d1), respectively. The scale bar is applied to all pictures.

### 3.4 Characteristics of YBCO nanostructures

To characterize the superconductivity of the ripple structures on YBCO thin films, the area of the ripple structure must be large enough to measure. Thus, the scanning scheme shown in Fig. 8 was adopted to prepare the large-area ripple structures on YBCO thin films. After passing through a variable neutral density filter, the beam was two-dimensionally scanned using a pair of galvanic mirrors with a speed of 7.6 cm/s. The laser beam was focused on the surface of the sample with a spot size of 220  $\mu\text{m}$  using an f-theta lens. All experiments were performed in air under atmospheric pressure.

It is evident from Fig. 16(g) that the quality of the crystalline structure of the YBCO films remained high after irradiation by the femtosecond laser with fluence up to 260 mJ/cm<sup>2</sup>. However, the quality deteriorated considerably with a further increase in laser fluences. For instance, with an irradiation fluence of 530 mJ/cm<sup>2</sup>, the intensity of the characteristic X-ray diffraction peaks diminished considerably. As shown in Fig. 17, while the superconductivity of the YBCO films remained nearly unchanged under low fluence irradiation, it began degrading at irradiation levels of 320 mJ/cm<sup>2</sup> and disappeared at 530 mJ/cm<sup>2</sup>, indicating structural and compositional changes with higher irradiation fluence.

As mentioned above, the crystalline structure of these YBCO nanodots induced by the laser irradiation ( $260 \text{ mJ/cm}^2$ ) remained oriented with the *c*-axis, with sharp diamagnetic Meissner effect characteristics at  $89.7 \text{ K}$  (Fig. 17), indicating that even after the dramatic morphological reconstruction, the obtained nanodots maintained most of their intrinsic properties. Indeed, as indicated by the energy dispersive spectroscopy (EDS) spectrum displayed in Fig. 16(h), which was taken on one of the nanodots [marked as area 1 in Fig. 16(e)], the composition of the nanodot had not changed from that of the original YBCO films. EDS results taken in the area between the dots [marked as area 2 in Fig. 16(e)] indicates no signal of Ba. Instead, traces of Al, presumably from the LAO substrate, were detected [see the second spectrum from the top in Fig. 16(h)]. This indicates that the composition of the area between any two nanodots has severely deviated from the stoichiometric composition of the original YBCO. The question is, how does this occur?

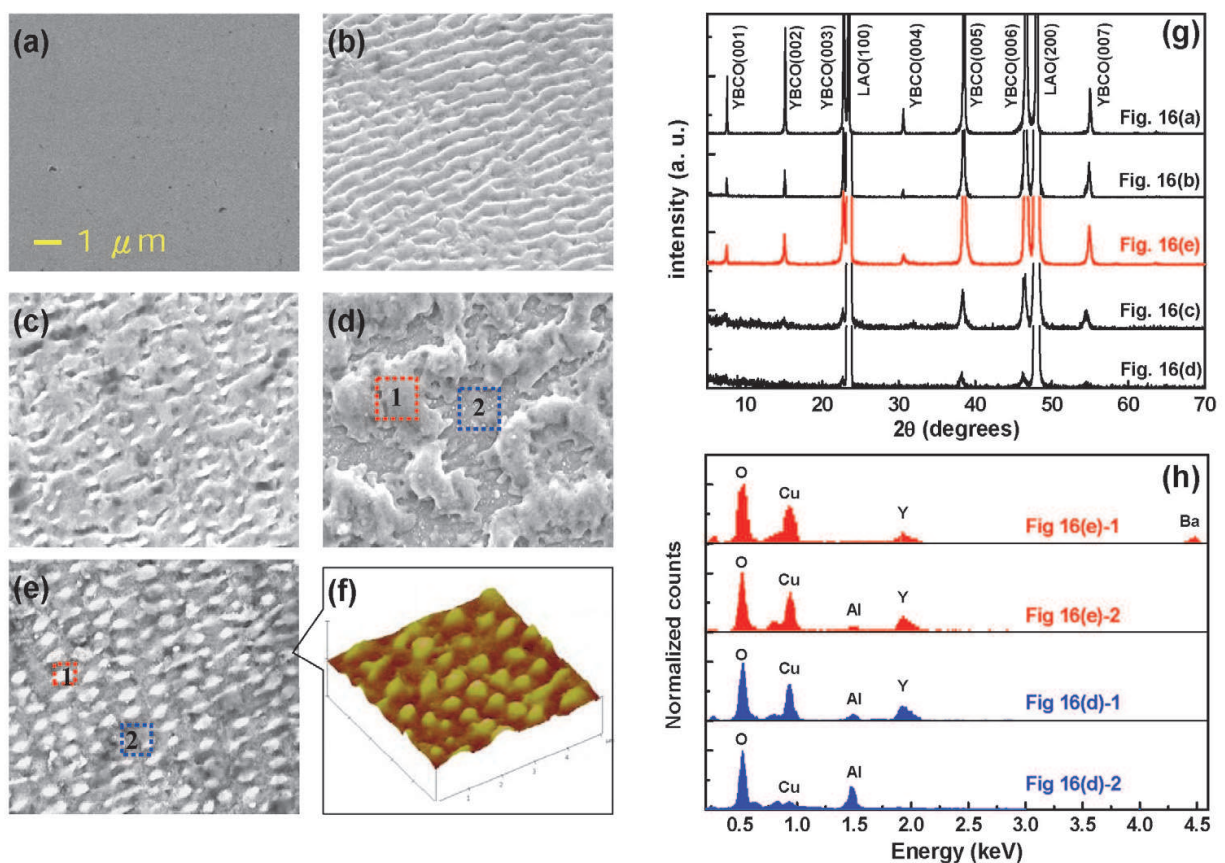


Fig. 16. (a) SEM images show the surface morphology of YBCO thin films at various laser fluences (a)  $F = 0 \text{ mJ/cm}^2$ , (b)  $F = 210 \text{ mJ/cm}^2$ , (c)  $F = 320 \text{ mJ/cm}^2$ , (d)  $F = 530 \text{ mJ/cm}^2$ , (e)  $F = 260 \text{ mJ/cm}^2$ . (f) AFM image of (e). (g) X-ray diffraction patterns of YBCO thin films at various laser fluences corresponding to (a)-(e). (h) EDS spectra show the composition of area 1 and area 2 in (d) and (e).

Due to the laser pulses, the transient increase in temperature,  $\Delta T$ , can be estimated using the following relation  $\Delta T = W / CV$ , where  $W$  is the pulse energy,  $C$  is the heat capacity, and  $V$  is the illuminated volume. For YBCO at  $300 \text{ K}$  using  $C = 2.86 \times 10^6 \text{ J/m}^3\text{K}$  [derived from the Debye heat capacity and the Debye temperature of YBCO was obtained from ref. (Stupp &

Ginsberg, 1989)],  $V = 1.14 \times 10^{-14} \text{ m}^3$  (the absorption length  $\sim 300 \text{ nm}$ ), and  $W$  on the order of  $0.1 \text{ mJ}$  (which is assumed to be totally absorbed by YBCO).  $\Delta T$  is approximately  $3000 \text{ K}$ . This increase in temperature, in principle, will lead to massive global melting of a thin layer beneath the surface of YBCO thin films. Thus, a more random pattern would be expected when re-solidified. However, due to the interference induced by the inhomogeneous input energy, the YBCO in melted phase initially forms ripples according to the interference pattern which pushes the YBCO to the line of destructive interference. This interference pattern also leads to a periodic distribution of the fluctuations in temperature,  $\Delta T$ , which happen to be higher than the boiling point of Ba [ $1897 \text{ K}$  (Thompson & Vaughan, 2001)] along the line of constructive interference and lower than the boiling point of Ba [ $1897 \text{ K}$  (Thompson & Vaughan, 2001)] along the line of destructive interference. As a result, in the regions of the constructive interference most Ba was vaporized, while in the destructive regions the Ba remained. Moreover, due to the surface tension and heterogeneous nucleation on the surface of the substrate, the melted YBCO along the lines of destructive interference aggregates to form nanodots in a periodic fashion, as shown in Fig. 16(b), 16(e), and 16(f). These results suggest that, by using single-beam femtosecond laser irradiation, it is possible to fabricate a self-organized array of YBCO nanodots with most of the crystallinity and superconducting properties remaining intact, provided proper control of irradiation fluence is practiced. This technique could potentially be applied to the fabrication of microwave filter devices with array structure or the weak-link Josephson junction arrays.

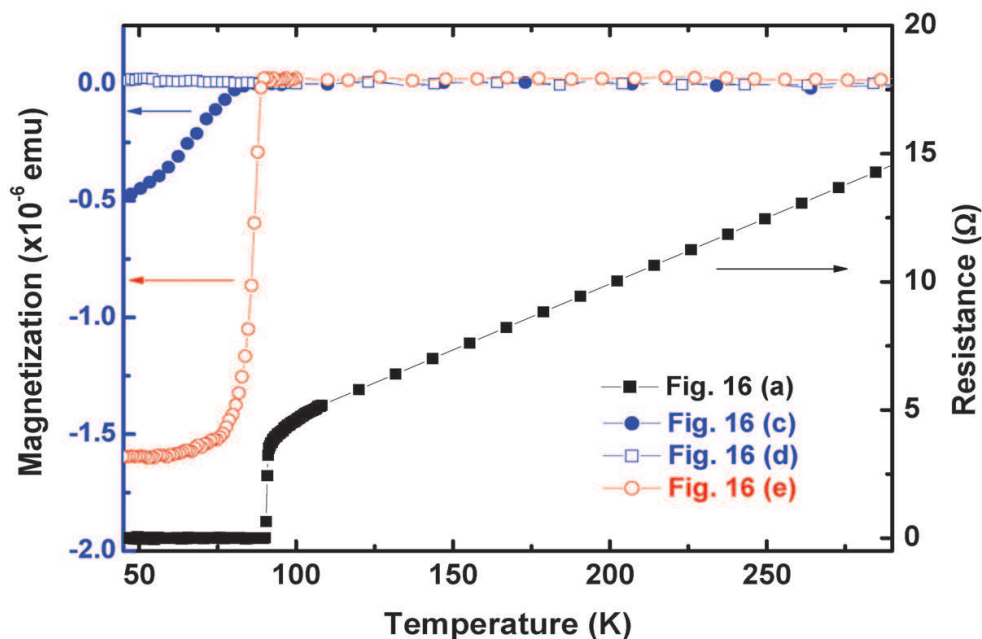


Fig. 17. Resistance versus temperature curve measured prior to femtosecond laser irradiation ( $F = 0 \text{ mJ}/\text{cm}^2$ ) and the magnetization versus temperature curve measured at  $10 \text{ Oe}$  after femtosecond laser irradiation, with various fluences corresponding to the Fig. 16 (c), 16(d), and 16(e), respectively.

Finally, as the fluence reached  $\geq 320$  mJ/cm<sup>2</sup>, irregular, disordered patterns were observed on the surface of the LAO substrate, as shown in Fig. 16(c) and Fig. 16(d). The characteristic XRD peaks of the (001)-YBCO films deteriorated significantly [Fig. 16(g)], indicating that the crystalline structure of YBCO had been destroyed by the higher laser fluence. EDS analysis [Fig. 16(h)] also shows that Ba was absent in both area 1 and area 2, marked in Fig. 16(d). In area 2, even the composition of Y is absent in the EDS spectrum. Using the previous estimation with  $W \geq 0.12$  mJ (fluence  $\geq 320$  mJ/cm<sup>2</sup>),  $\Delta T \geq 3700$  K was obtained, which is higher than the boiling point of Ba [1897 K (Thompson & Vaughan, 2001)] at the positions of both constructive and destructive interference, but only higher than the boiling point of Y [3345 K (Thompson & Vaughan, 2001)] at the position of constructive interference. In this case, the aggregation of melted YBCO becomes more disordered and the stoichiometric composition is more severely influenced, leading to the loss of crystalline integrity and superconductivity in the remaining residue of the original YBCO film.

#### 4. Conclusions

In this chapter, we demonstrated a simple, rapid means to obtain the hexagonal ZnSe nanoparticles, YBCO ripples, and dot structures. In the fabrication of ZnSe nanoparticles, while femtosecond laser pulses were focused on the surface of ZnSe wafers in air and the ablated plume cannot expand as rapidly as plumes would in a vacuum chamber which causes an instantaneous high-energy, high-pressure region around the focal point of the laser; meanwhile, a large amount of spherical-shape ZnSe nanoparticles with an average diameter of 16-22 nm (depending on the laser fluence) forms on the surface of the wafer. During the formation of ZnSe nanoparticles, the structural phase further changes from cubic to metastable hexagonal phase due to the ultrahigh localized ablation pressure caused by the rapid injection of high laser energy within a femtosecond time scale.

For the generation of ripple and dot structures, we have systematically studied the surface morphology of YBCO thin films under a single-beam and a dual-beam fs laser irradiation. The generation of ripple and dot periodic structures was determined by the applied laser fluence, number of pulses, and polarization of the laser. The period and orientation of ripples, and even the size and density of dots can be controlled by these parameters. With lower laser fluence, the (001)-YBCO film turns into (001)-ripple or dot arrays with superconductivity remaining nearly intact. These rippled (or dotted) structures and superconductivity, however, were rapidly destroyed with higher fluence. These results may be applied to enhance the critical current of YBCO thin films and the fabrication of the microwave filter devices with array structures or the weak-link Josephson junction arrays.

The present results clearly demonstrate that the femtosecond laser, in addition to its crucial role in studying the ultrafast dynamics of matter, they can also serve as a new avenue for engineering materials and structures into their surfaces at a nanometer scale.

#### 5. Acknowledgments

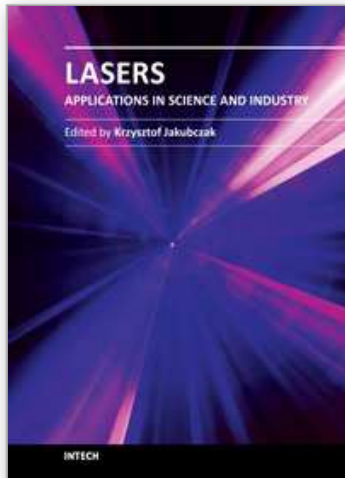
The author would like to express his sincere appreciation and gratitude to his collaborators and colleagues, Ms. H. I. Wang, Mr. W. T. Tang, Ms. C. C. Lee, and Mr. L. W. Liao, Profs. T. Kobayashi, K. H. Wu, J. Y. Juang, J.-Y. Lin, T. M. Uen, C. S. Yang. This work was supported by the MOE-ATU program at NCTU and National Science Council of Taiwan, under Grant No. NSC 98-2112-M-009-008-MY3.

## 6. References

- Amoruso, S.; Bruzzese, R.; Spinelli, N.; Velotta, R.; Vitiello, M.; Wang, X.; Ausanio, G.; Lannotti, V. & Lanotte, L. (2004). Generation of Silicon Nanoparticles via Femtosecond Laser Ablation in Vacuum. *Applied Physics Letters*, Vol.84, No.22, (May 2004) pp. 4502-4504, ISSN 0003-6951
- Batani, D.; Stabile, H.; Ravasio, A.; Lucchini, G.; Strati, F.; Desai, T.; Ullschmied, J.; Krousky, E.; Skala, J.; Juha, L.; Kralikova, B.; Pfeifer, M.; Kadlec, Ch.; Mocek, T.; Präg, A.; Nishimura, H. & Ochi, Y. (2003). Ablation pressure scaling at short laser wavelength. *Physical Review E*, Vol.68, No.6, (December 2003) pp. 067403, ISSN 1539-3755
- Bonse, J. & Krüger, J. (2010). Pulse Number Dependence of Laser-Induced Periodic Surface Structures for Femtosecond Laser Irradiation of Silicon. *Journal of Applied Physics*, Vol.108, No.3, (August 2010) pp. 034903, ISSN 0021-8979
- Che, J.; Yao, X.; Jian, H. & Wang, M. (2004). Application and preparation of ZnSe nanometer powder by reduction process. *Ceramics International*, Vol.30, No.7, (July 2004) pp. 1935-1938, ISSN 0272-8842
- Dinger, A.; Becker, R.; Goppert, M.; Petillon S.; Grun, M.; Klingshirm, C.; Liang, J.; Wagner, V. & Geurts, J. (2000). Lattice dynamical properties of cubic CdS/ZnSe strained-layer superlattices. *Journal of Crystal Growth*, Vol.214, No.2, (June 2000) pp. 676-679, ISSN 0022-0248
- Groot, J. S. De; Estabrook, K. G.; Kruer, W. L.; Drake, R. P.; Mizuno, K. & Cameron, S. M. (1992). Distributed absorption model for moderate to high laser powers. *Physics of Fluids B*, Vol.4, No.3, (March 1992) pp. 701-707, ISSN 0899-8221
- Greene, R. G.; Luo, H. & Ruoff, A. L. (1995). High pressure x-ray and raman study of ZnSe. *Journal of Physics and Chemistry of Solids*, Vol.56, No.3/4, (March-April 1995) pp. 521-524, ISSN 0022-3697
- Hsu, E. M.; Crawford, T. H. R.; Tiedje, H. F. & Haugen, H. K. (2007). Periodic Surface Structures on Gallium Phosphide after Irradiation with 150 fs-7 ns Laser Pulses at 800 nm. *Applied Physics Letters*, Vol.91, No.11, (September 2007) pp. 111102, ISSN 0003-6951
- Huang, M.; Zhao, F.; Cheng, Y.; Xu, N. & Xu, Z. (2009). Origin of Laser-Induced Near-Subwavelength Ripples: Interference between Surface Plasmons and Incident Laser. *ACS Nano*, Vol.3, No.12, (November 2009) pp. 4062-4070, ISSN 1936-0851
- Jiang, Y.; Meng, X. M.; Yiu, W. C.; Liu, J.; Ding, J. X.; Lee, C. S. & Lee, S. T. (2004). Zinc Selenide Nanoribbons and Nanowires. *The Journal of Physical Chemistry B*, Vol.108, No.9, (March 2004) pp. 2784-2787, ISSN 1520-6106
- Jia, T. Q.; Zhao, F. L.; Huang, M.; Chen, H. X.; Qiu, J. R.; Li, R. X.; Xu, Z. Z. & Kuroda, H. (2006). Alignment of Nanoparticles Formed on the Surface of 6H-SiC Crystals Irradiated by Two Collinear Femtosecond Laser Beams. *Applied Physics Letters*, Vol.88, No.11, (March 2006) pp. 111117, ISSN 0003-6951
- Jia, X.; Jia, T. Q.; Zhang, Y.; Xiong, P. X.; Feng, D. H.; Sun, Z. R.; Qiu, J. R. & Xu, Z. Z. (2010). Periodic Nanoripples in the Surface and Subsurface Layers in ZnO Irradiated by Femtosecond Laser Pulses. *Optics Letters*, Vol.35, No.8, (April 2010) pp. 1248-1250, ISSN 0146-9592

- Key, M. H.; Rumsby, P. T.; Evans, R. G.; Lewis, C. L. S.; Ward, J. M. & Cooke, R. L. (1980). Study of Ablatively Imploded Spherical Shells. *Physical Review Letters*, Vol.45, No.22, (December 1980) pp. 1801-1804, ISSN 0031-9007
- Liu, B.; Hu, Z.; Che, Y.; Chen, Y. & Pan, X. (2007a). Nanoparticle generation in ultrafast pulsed laser ablation of nickel. *Applied Physics Letters*, Vol.90, No. 4, (January 2007) pp. 44103, ISSN 0003-6951
- Liu, S. Y.; Choy, W. C. H.; Jin, L.; Leung, Y. P.; Zheng, G. P.; Wang, J. & Soh, A. K. (2007b). Triple-Crystal Zinc Selenide Nanobelts. *The Journal of Physical Chemistry C*, Vol.111, No.26, (July 2007) pp. 9055-9059, ISSN 1932-7447
- Liu, S. Y.; Choy, W. C. H.; Jin, L.; Leung, Y. P.; Zheng, G. P.; Wang, J. & Soh, A. K. (2007). Triple-Crystal Zinc Selenide Nanobelts. *The Journal of Physical Chemistry C*, Vol.111, No.26, (July 2007) pp. 9055-9059, ISSN 1932-7447
- Luo, C. W.; Lee, C. C.; Li, C. H.; Shih, H. C.; Chen, Y.-J.; Hsieh, C. C.; Su, C. H., Tzeng, W. Y.; Wu, K. H.; Uen, T. M.; Juang, J. Y.; Chen, S. P.; Lin, J.-Y. & Kobayashi, T. (2008). Ordered YBCO Sub-Micron Array Structures Induced by Pulsed Femtosecond Laser Irradiation. *Optics Express*, Vol.16, No.25, (December 2008) pp. 20610-20616, ISSN 1094-4087
- Martienssen, W. & Warlimont, H. (2005). *Springer Handbook of Condensed Matter and Materials Data*, Heidelberg: Springer-Verlag, Berlin
- Nayak, B. K.; Gupta, M. C. & Kolasinski, K. W. (2008). Formation of Nano-Textured Conical Microstructures in Titanium Metal Surface by Femtosecond Laser Irradiation. *Applied Physics A: Materials Science & Processing*, Vol.90, No.3, (December 2007) pp. 399-402, ISSN 0947-8396
- Okamuro, K.; Hashida, M.; Miyasaka, Y.; Ikuta, Y.; Tokita, S. & Sakabe, S. (2010). Laser Fluence Dependence of Periodic Grating Structures Formed on Metal Surfaces under Femtosecond Laser Pulse Irradiation. *Physical Review B*, Vol.82, No.16, (October 2010) pp. 165417, ISSN 1098-0121
- Rudolph, P.; Schäfer, N. & Fukuda, T. (1995). Crystal growth of ZnSe from the melt. *Materials Science and Engineering: R: Reports*, Vol.15, No.3, (September 1995) pp. 85-133, ISSN 0927-796X
- Stupp, S. E. & Ginsberg, D. M. (1989). A review of the linear term in the low temperature specific heat of  $\text{YBa}_2\text{Cu}_3\text{O}_{7-\delta}$ . *Physica C* Vol.158, No.3, (May 1989) pp. 299-310, ISSN 0921-4534
- Stuart, B. C.; Feit, M. D.; Rubenchik, A. M.; Shore, B. W. & Perry, M. D. (1995). Laser-Induced Damage in Dielectrics with Nanosecond to Subpicosecond Pulses. *Physical Review Letters*, Vol.74, No.12, (March 1995) pp. 2248-2251, ISSN 0031-9007
- Sarigiannis, D.; Peck, J. D., Kioseoglou, G.; Petrou, A. & Mountziaris, T. J. (2002). Characterization of Vapor-Phase-Grown ZnSe nanoparticles. *Applied Physics Letters*, Vol.80, No.21, (May 2002) pp. 4024-4026, ISSN 0003-6951
- Shimotsuma, Y.; Kazansky, P. G.; Qiu, J. & Hirao, K. (2003). Self-Organized Nanogratings in Glass Irradiated by Ultrashort Light Pulses. *Physical Review Letters*, Vol.91, No.24, (December 2003) pp. 247405, ISSN 0031-9007
- Shan, C. X.; Liu, Z.; Zhang, X. T.; Wong, C. C. & Hark, S. K. (2006). Wurtzite ZnSe nanowires: growth, photoluminescence, and single-wire Raman properties. *Nanotechnology*, Vol.17, No.22, (November 2006) pp. 5561-5564, ISSN 0957-4484

- Sakabe, S.; Hashida, M.; Tokita, S.; Namba, S. & Okamuro, K. (2009). Mechanism for Self-Formation of Periodic Grating Structures on a Metal Surface by a Femtosecond Laser Pulse. *Physical Review B*, Vol.79, No.3, (January 2009) pp. 033409, ISSN 1098-0121
- Tseng, K. Y.; Wong, K. S. & Wong, G. K. L. (1996). Femtosecond Time-Resolved Z-scan Investigations of optical nonlinearities in ZnSe. *Optics Letters*, Vol.21, No.3, (February 1996) pp. 180-182, ISSN 0146-9592
- Tawara, T.; Tanaka, S.; Kumano, H. & Suemune, I. (1999). Growth and luminescence properties of self-organized ZnSe quantum dots. *Applied Physics Letters*, Vol.75, No.2, (July 1999) pp. 235-237, ISSN 0003-6951
- Thompson, A. C. & Vaughan, D. (2001). *X-ray data booklet*, Lawrence Berkeley National Laboratory, California, USA
- Tsuji, T.; Kakita, T. & Tsuji, M. (2003). Preparation of Nano-Size Particles of Silver with Femtosecond Laser Ablation in Water. *Applied Surface Science*, Vol.206, No.1-4, (February 2003) pp. 314-320, ISSN 0169-4332
- Teng, Y.; Zhou, J.; Luo, F.; Ma, Z.; Lin, G. & Qiu, J. (2010). Shape- and Size-Controllable Microstructure on Glass Surface Induced by Femtosecond Laser Irradiation. *Optics Letters*, Vol.35, No.13, (July 2010) pp. 2299-2301, ISSN 0146-9592
- Xiang, B.; Zhang, H. Z.; Li, G. H.; Yang, F. H.; Su, G. H.; Wang, R. M.; Xu, J.; Lu, G. W.; Sun, X. C.; Zhao, Q. & Yu, D. P. (2003). Green-light-emitting ZnSe nanowires fabricated via vapor phase growth. *Applied Physics Letters*, Vol.82, No.19, (May 2003) pp. 3330-3332, ISSN 0003-6951
- Yang, Y.; Yang, J.; Xue, L. & Guo, Y. (2010). Surface Patterning on Periodicity of Femtosecond Laser-Induced Ripples. *Applied Physics Letters*, Vol.97, No.14, (October 2010) pp. 141101, ISSN 0003-6951
- Zhou, G.; Fauchet, P. M. & Siegman, A. E. (1982). Growth of spontaneous periodic surface structures on solids during laser illumination. *Physical Review B*, Vol.26, No.10, (November 1982) pp. 5366-5381, ISSN 1098-0121
- Zhao, Q. Z.; Malzer, S. & Wang, L. J. (2007a). Formation of subwavelength periodic structures on tungsten induced by ultrashort laser pulses. *Optics Letters*, Vol.32, No.13, (July 2007) pp. 1932-1934, ISSN 0146-9592
- Zhao, Q. Z.; Malzer, S. & Wang, L. J. (2007b). Self-Organized Tungsten Nanospikes Grown on Subwavelength Ripples Induced by Femtosecond Laser Pulses. *Optics Express*, Vol.15, No.24, (November 2007) pp. 15741-15746, ISSN 1094-4087



## **Lasers - Applications in Science and Industry**

Edited by Dr Krzysztof Jakubczak

ISBN 978-953-307-755-0

Hard cover, 276 pages

**Publisher** InTech

**Published online** 09, December, 2011

**Published in print edition** December, 2011

The book starts with basic overview of physical phenomena on laser-matter interaction. Then it is followed by presentation of a number of laser applications in the nano-particles and thin films production, materials examination for industry, biological applications (in-vitro fertilization, tissue ablation) and long-range detection issues by LIDARs.

### **How to reference**

In order to correctly reference this scholarly work, feel free to copy and paste the following:

Chih Wei Luo (2011). Nanoparticles and Nanostructures Fabricated Using Femtosecond Laser Pulses, Lasers - Applications in Science and Industry, Dr Krzysztof Jakubczak (Ed.), ISBN: 978-953-307-755-0, InTech, Available from: <http://www.intechopen.com/books/lasers-applications-in-science-and-industry/nanoparticles-and-nanostructures-fabricated-using-femtosecond-laser-pulses>

**INTECH**  
open science | open minds

### **InTech Europe**

University Campus STeP Ri  
Slavka Krautzeka 83/A  
51000 Rijeka, Croatia  
Phone: +385 (51) 770 447  
Fax: +385 (51) 686 166  
[www.intechopen.com](http://www.intechopen.com)

### **InTech China**

Unit 405, Office Block, Hotel Equatorial Shanghai  
No.65, Yan An Road (West), Shanghai, 200040, China  
中国上海市延安西路65号上海国际贵都大饭店办公楼405单元  
Phone: +86-21-62489820  
Fax: +86-21-62489821

© 2011 The Author(s). Licensee IntechOpen. This is an open access article distributed under the terms of the [Creative Commons Attribution 3.0 License](#), which permits unrestricted use, distribution, and reproduction in any medium, provided the original work is properly cited.

IntechOpen

IntechOpen